Biophysical Journal Volume 77 August 1999 865–878

Actin Protofilament Orientation at the Erythrocyte Membrane

Catherine Picart* and Dennis E. Discher*#§

Institute for Medicine and Engineering, and Departments of §Mechanical, #Chemical, and *Bio-Engineering, University of Pennsylvania, Philadelphia, Pennsylvania 19104-6315

ABSTRACT The short actin filaments in the erythrocyte's membrane skeleton are shown to be largely oriented tangent to the lipid bilayer. Actin "proto"-filaments have previously been described as junctional centers intertriangulated by spectrin; however, the protofilaments may simultaneously serve as pinning centers between the network and the overlying bilayer. The latter function now seems of particular importance because near-normal network assembly has been reported with transgenic mouse sphero-erythrocytes that lack the primary linkage protein Band 3. To assess possible physical constraints on actin protofilaments in intact membranes, fluorescence polarization microscopy (FPM) has been used to study rhodamine phalloidin-labeled red cell ghosts. A basis for interpreting FPM images of cells is provided by FPM applied to isolated actin filaments. These are labeled with the same rhodamine probes and imaged at various orientations with respect to the polarizers, including filament orientations perpendicular to the image plane. High aperture and fluorophore conjugation effects are found to be minimal, enabling development of a simple, semi-empirical model which indicates that protofilaments are generally within ~20° of the membrane tangent plane.

INTRODUCTION

Filamentous actin is a nearly universal contributor to cell membrane structure. The red cell membrane is no exception; short actin protofilaments (~13–15 subunits) in this membrane's skeleton constitute central nodes for cross-linking by spectrin (Fig. 1 *A*) (Byers and Branton, 1985; Shen et al., 1986; Ursitti and Fowler, 1994). The importance of this network structure to red cell function is evident in the component defects and deficiencies associated with easily fragmentable membranes and anemias (e.g., Waugh and Agre, 1988; Mohandas and Evans, 1994). F-actin is also found at many other membranes, in varying degrees of orientational order. In the cylindrically-shaped outer hair cell, for example, long actin filaments lie tangent to the membrane, wrapping circumferentially around the cell and preferentially stiffening that direction (Holley and Ashmore, 1990). Similar, ~2-dimensional-nematic ordering of F-actin has also been documented in pure lipid membrane systems, at least at low ionic strength (Gicquaud et al., 1995; Grimm et al., 1997). In contrast, quasi-isotropic distributions of actin filaments occur in cortical shells of both neutrophils (e.g., Ting-Beall et al., 1995) and amoeba (Stockem et al., 1983). Whether actin protofilaments at the erythrocyte membrane are randomly directed or, perhaps, oriented at fixed, average angles with respect to the membrane is the central focus of this study. The results should prove important to understanding both the molecular mechanisms of network-membrane attachment and the microstructural basis for membrane deformability.

The essential physical variable at issue is the angle, θ_i, which the *i*th actin protofilament makes with respect to the lipid bilayer's local tangent plane. Defining this angle is a half-helix protofilament of length ~35 nm (Byers and Branton, 1985; Fowler, 1996). Such a length appears consistent with estimates of the total actin present in the cell divided by the number of spectrin-actin nodes ($\sim 3 \times 10^4$) in the triangulated network. Furthermore, since the protofilament length is ~100-times smaller than the persistence length of F-actin (Kas et al., 1996), the protofilaments may be considered rigid. However, the protofilament length is also a significant fraction of the inter-actin separation of ~60–80 nm (Byers and Branton, 1985). In network deformation, where stretching and contraction may both reach a factor of two or more (Discher and Mohandas, 1996), local protofilament orientation may therefore strongly modulate, and perhaps frustrate, spectrin rearrangement. Conversely, since spectrin has a persistence length that is a small fraction of its contour length (~200 nm; Stokke et al., 1986), the Brownian motion of many spectrin segments bound to an actin protofilament might very well influence protofilament orientation in both deformed and undeformed states.

The protofilament angle θ_i should reflect, more specifically, the modes of interaction between the network and the overlying bilayer. Band 3 has long been considered to be the primary site for pinning the network to the lipid bilayer (e.g., Bennett and Stenbuck, 1979). However, Band 3-deficient erythrocytes have near-normal networks assembled at their membranes, despite the spherocytic appearance and reduced stability of these cells (Peters et al., 1996; Southgate et al., 1996). Glycophorin C, via protein 4.1, appears to provide a second important site of network attachment to the membrane. Glycophorin C is present at $\sim 2 \times 10^5$ molecules per cell (Smythe et al., 1994) and binds protein 4.1 with moderate affinity (Pinder et al., 1995; Reid et al., 1990). Protein 4.1 is present in similar number and also

Received for publication 16 September 1998 and in final form 5 May 1999.

Address reprint requests to Dr. Dennis Discher, Towne Bldg. 112, University of Pennsylvania, 220 S. 33rd St., Philadelphia, PA 19104-6315. Tel.: 215-898-4825; Fax: 215-573-6334; E-mail: discher@seas.upenn.edu.

0006-3495/99/08/865/14 $2.00

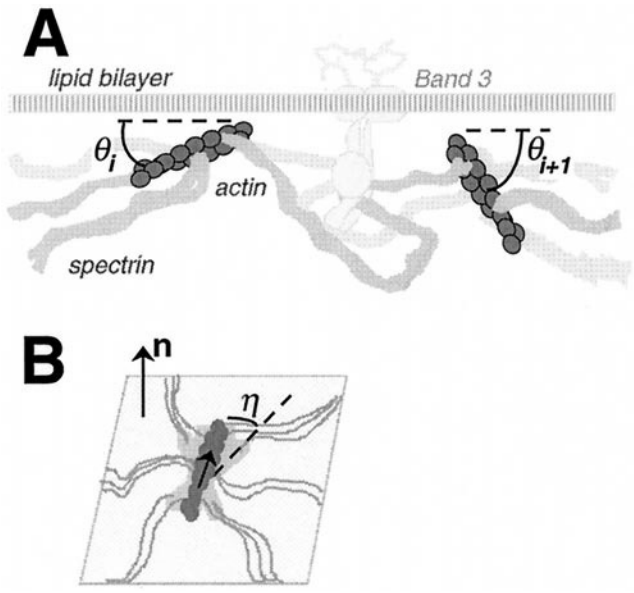

FIGURE 1 Side- and top-view schematics of actin protofilaments in the red cell membrane. (*A*) Scaled side view. Omitted are many integral and peripheral membrane proteins, particularly protein 4.1 and Glycophorin C that are implicated in anchoring the actin filaments to the overlying bilayer. Actin protofilaments are helical and of length ~35 nm; the *i*th filament makes an angle θ_i with respect to the bilayer's local tangent plane. (*B*) Coarse top view of network in thermal motion with identification of the azimuthal angle η around the membrane normal **n**.

functions as a critical stabilizer of spectrin–actin interactions (Tyler et al., 1979). Among the most convincing results in support of a simultaneous actin·4.1·glycophorin C linkage is that glycophorin C is retained by the spectrin-actin-4.1 skeleton after detergent extraction of lipid from normal cells. Glycophorin C is not, in contrast, retained in 4.1-deficient cell skeletons (Reid et al., 1990). However, glycophorin C-deficient membranes have near-normal elasticity (Nash et al., 1990), despite evidence for a slight deficiency of protein 4.1 (Alloisio et al., 1993). Finally, given the fact that actin is held to have simultaneous interactions with spectrin, perhaps the lipid bilayer (Pradhan et al., 1991), as well as many other proteins in the red cell (e.g., adducin; Mische et al., 1987), it could be that these latter interactions also strongly influence actin orientation.

Fluorescence polarization microscopy (FPM) is an extremely powerful method for addressing issues of molecular orientation in cells. The first application to red cells appears to have been the determination of the orientation of the lipid analog diI (1.1′ dioctadecyl-3,3,3′,3′-tetramethyl-indocarbocyanine perchlorate) at the plasma membrane (Axelrod, 1979). More recently, confocal FPM has been applied to the study of eosin-5-maleimide attached to Band 3, thereby showing the surface-tangent orientation of this specific probe (Blackman et al., 1996). In application of FPM to cytoskeletal molecules in other cell types, myosin orientation has been particularly well studied, with current efforts focused on precisely conjugated fluorescent moieties (e.g., Sabido-David et al., 1998). The orientation of actin filaments in nonerythroid cells has also been studied by making use of the approximate alignment between the filament axis and the dipoles of actin-bound rhodamine phalloidin (Kinosita et al., 1991; Zhukarev et al., 1995). At the erythrocyte membrane, the orientations and rotations of network protofilaments should reflect molecular mechanisms of interaction with membrane components and would also seem physically likely to contribute to membrane elasticity.

The content of the paper is organized as follows. The next section highlights technical details of the experimental methods and concludes with a calibration study of diI on sphered red cells that examines high aperture effects in FPM. The subsequent section then presents FPM results for rhodamine phalloidin-labeled actin filaments in red cell ghosts, examining the effects of both aperture and probe attachment chemistry. This is followed by FPM applied to isolated actin filaments labeled with the same probes. Based on these latter calibrating results, the subsequent discussion presents discrete and probabilistic determinations of the protofilament angle θ at the membrane of sphered cells. A conclusion section summarizes this discussion and suggests further avenues for understanding the role of actin orientation in both undeformed and deformed cells.

MATERIALS AND METHODS

Labeling of membrane F-actin by rhodamine phalloidin

Rhodamine phalloidin was purchased either from Molecular Probes (Eugene, OR) or Sigma (St. Louis, MO); the two compounds differ as shown in Fig. 2, *A* and *B*. The isotype from Molecular Probes, designated hereafter by MP, has a shorter linking group between phalloidin's seventh residue, dihydroxyleucine, and the fluorescent group, tetramethylrhodamine-5-isothiocyanate (5-TRITC). The isotype from Sigma is a mixture of stereoisomers reportedly synthesized by the method of Faulstich et al. (1988). In addition to the four stereoisomers arising from the two chiral carbons, a mixture of both 5- and 6-TRITC is conjugated to phalloidin. Separation of the stereo-isomers appeared achievable by thin layer chromatography on a silica gel plate (Fig. 2 *C*) following prior techniques (Faulstich et al., 1988). Only the largest peak, peak 2, was scraped from the plate, dissolved into methanol, and collected for labeling of both isolated actin filaments and cell membranes.

To label the internal skeletal network, red cells were reversibly permeabilized by cold, hypotonic lysis allowing affinity probes in the lysis buffer to diffuse into the permeabilized cell ghost and bind internally (Takakuwa et al., 1986; Lieber and Steck, 1989; Discher et al., 1995). Labeling of skeletal actin with rhodamine phalloidin was accomplished by first air-drying (2.5 μL of 1 mg/mL in MeOH) and then redissolving the phalloidin in 10 μL of cold lysis buffer (10 mM phosphate, pH 7.4 $\pm$ 0.1). Cold, packed red cells (5 μL) were added, and, after 10 min, the suspension was made 100 mM in KCl, 1 mM in $MgCl_2$ and then warmed at 37°C for 30 min. This procedure gave pink ghosts; results from whiter ghosts made with 15 μL of lysis buffer were within measurement error. Axelrod (1979) also reported minimal difference between cells and ghosts. Mechanical properties of such resealed membranes are not significantly altered by the labeling procedure (Discher et al., 1996), and a concentration-dependent edge-brightness has indicated an apparent, in situ $K_a \sim 3 \times 10^6$ M (Discher et al., 1995), which is only slightly less than in vitro assays. Rhodamine phalloidin is not able to fluorescently label unlysed cells. Labeled cell ghosts were sphered with PBS/BSA (10 mg/mL) prediluted ~1:2.5 with distilled water.

Polymerization and labeling of isolated actin

Rabbit muscle G-actin was either purified from an acetone powder of rabbit skeletal muscle (generously provided by Dr. Thomas Giseler) or purchased as 99% pure form in buffered solution from Cytoskeleton, Inc. (Denver, CO). G-actin was stored frozen at −70°C until use. To polymerize G-actin, 10 mg/mL G-actin solution was diluted 1:100 into buffer A (300 mM KCl, 10 mM $MgCl_2$, 40 mM PBS, 0.05 mM β-mercaptoethanol) prediluted to 25% with deionized water. This was added to raise the ionic strength and initiate polymerization. After incubation of the actin at room temperature for 10 min, 100 μL of actin was added to a tube containing rhodamine phalloidin that had been dried under Argon from 45 μL (7 μM phalloidin in ethanol). The sample was incubated at 4°C for 5 min and centrifuged for one hour at 80,000 rpm and 4°C. The supernatant was removed and pelleted filaments were resuspended in buffer containing an oxygen depletion system (Kishino and Yanagida, 1988). This deoxygenation buffer is the standard F-actin buffer containing, in addition, 2.3 mg/mL glucose, 0.018 mg/mL glucose oxidase, 0.1 mg/mL catalase (Sigma, St. Louis, MO). The chamber for observation was assembled from a microscope slide coated with poly-[sc]l-lysine (0.01% w/v in water) and sealed with melted parafilm, silicone vacuum grease, and a coverslip.

Fluorescence polarization microscope

Image collection was accomplished through the side-port of an infinity-corrected Nikon TE-300 inverted fluorescence microscope connected via a 10× magnification lens to a Photometrics (Tucson, AZ) CH360 cooled, back-thinned charge coupled device (CCD) camera controlled by Image Pro (Silver Spring, MD) software run on a Pentium 200 MHz PC. Mounted between the microscope's 100W-Hg excitation lamp and the dichroic reflector was a three-holed slider with both vertically and horizontally oriented polarizers (Meadowlark Optics, Denver, CO). Mounted between the emission filter and the CCD was a second, similar slider. This simple configuration of insertable sliders for FPM is essentially as described by Zhukarev et al. (1995). The excitation lamp was shuttered (Uniblitz from Vincent Associates, Rochester, NY) to synchronize excitation with a second shutter exposing the CCD; the typical exposure time was set between 200 and 300 msec. The CCD is essentially the same as that used in previous studies of fluorescence imaged microdeformation (Discher et al., 1994). It is well known for its linearity of intensity versus signal and, at the emission wavelengths of rhodamine, it has a quantum efficiency in excess of 80%. Either a strain-free 40×, 1.0 NA or a strain-free 60×, 1.4 NA objective was used, and, for both objectives, the immersion oil, which optically coupled the lens to the coverslip, had a refractive index, n, of 1.52.

Four different polarization images were acquired with the four possible pairs of excitation and emission polarizers: two images were taken with parallel polarizers—both horizontal or both vertical, and two images were taken with crossed polarizers—excitation vertical and emission horizontal, or the reverse. Collected images were analyzed using either Image Pro or National Institutes of Health Image software. Background subtractions were made as required. Systematic polarization introduced by the microscope optics was evaluated with a randomly oriented, immobilized fluorophore as described elsewhere (Axelrod, 1979). Intensity correction factors of 4–11% were derived, dependent on the objective lens and the polarizer pair. To simplify notation, we denote emission and excitation polarizers that are both parallel by ∥, and emission and excitation polarizers that are both crossed by ⊥. When object symmetry permitted, such as with sphered red cells, image intensities were averaged for like polarizer orientations. Such averaging could not be done for imaging single filaments, which obviously break rotational invariance about the optical axis of the microscope. To deal with such cases of symmetry breaking and, as clarified below, we will introduce a coordinate frame analogous to that of Axelrod (1979): X_1 is the optical axis and X_3 is always the direction of excitation polarization. An actin filament, for example, can be oriented in any direction with respect to these optically defined axes, and changing excitation polarizers will change the defined optical frame even though the filament is stationary in the lab frame. This will be further clarified in the Results. Experiments were done at ~23°C unless otherwise noted.

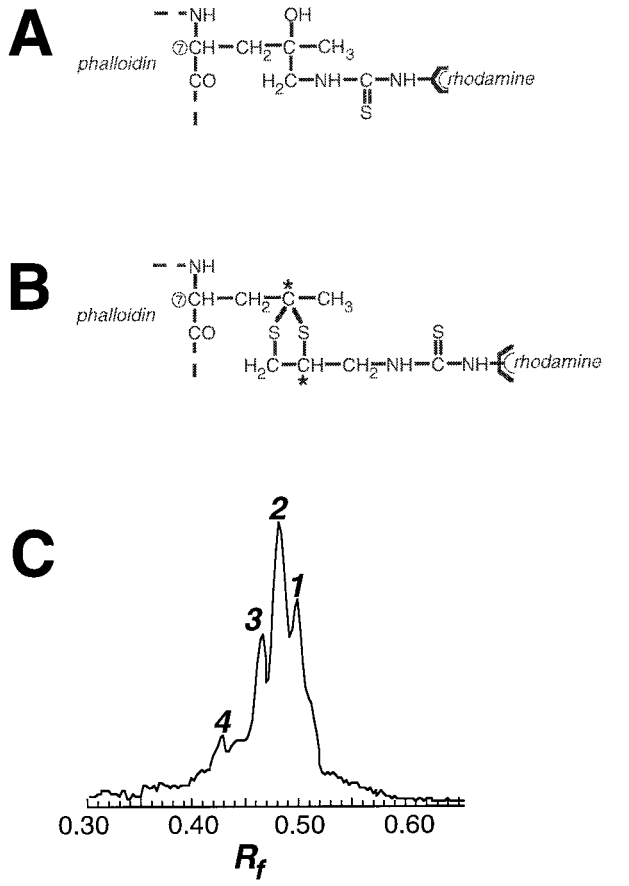

FIGURE 2 Rhodamine phalloidin used to label actin filaments. (*A*) Major rhodamine phalloidin isotype MP. (*B*) Major rhodamine phalloidin isotype(s) from Sigma, containing two chiral carbons designated with asterisks. (*C*) Thin layer chromatography separation of four major stereoisomers of rhodamine phalloidin in the Sigma mixture. The relative migration from the point of mixture application is expressed as a ratio with respect to the solvent front.

FPM of diI-labeled and sphered ghosts

Depolarization introduced by high aperture objectives was theoretically studied by Axelrod (1979) in what appears to be the first published FPM study of a fluorescent molecule, diI, in the red cell membrane. DiI is a lipid analog that labels the lipid bilayer and was shown to orient with its headgroup parallel to the bilayer surface. The cited experiments used a laser as a polarized excitation source together with high numerical aperture (NA) optics and a ray optics theory for correcting high NA effects. Omitted from this groundbreaking study was any experimental verification of the theoretical dependence of high NA optics.

To compare our system with its Hg-lamp excitation through polarizers to laser-based systems, and to also test the NA corrections as theoretically formulated by Axelrod, sphered red cells were labeled with diI and studied by FPM. In addition to the NA 1.0 and NA 1.4 oil immersion objectives, a 40× air objective with NA = 0.75 was also used in these experiments with diI. For labeling red cells with diI, 2.5 μL of packed cells were added to 1.5 μL of 0.6 mg/mL diI in methanol. The suspension was incubated for 15 min at 37°C, followed by centrifugation at 1500 × g for 4 min. The supernatant was removed and the cells resuspended in PBS/BSA (10

mg/mL) that had been diluted 1:2.5 with distilled water. DiI-labeled cells and their ghosts give comparable results in FPM (Axelrod, 1979).

The dilute suspension was viewed in an open-sided chamber, and polarization images were collected by focusing in the equatorial plane of the sphere as schematically shown in Fig. 3. The regions *B* and *C* at the membrane correspond to pixeled areas in the image of dimension ~300 × 300 nm. In the absence of polarizers that break spherical symmetry, the fluorescence intensities from labeled lipids at any two such edge points of a sphere's image have previously been reported to be equal within 10% (Discher et al., 1994). With polarizers, following Axelrod, the excitation direction is taken to always define the X_3-direction. Point *C* is then always identified as the point where X_3 is tangent to the sphere. Point *A* contributes signal to the center of an image and so does the point on the sphere antipodal to point *A*. Again following the analysis of Axelrod, intensity ratios were formed between the three points *A*, *B*, and *C*, and averages are reported in Fig. 4. Symmetry was used where possible, and results for appropriate pairs of polarizers were combined. For example, the ratio denoted as $F_{\parallel}^{A}/F_{\perp}^{A}$ includes intensities from point *A* on cell images as obtained with (i) horizontal excitation and emission polarizers divided by horizontal excitation polarizer and vertical emission polarizer, and also (ii) vertical excitation and emission polarizers ratioed against vertical excitation polarizer and horizontal emission polarizer. Note that, in both ratios, the intensity of the numerator derives from parallel polarizers, as specified by the notation.

The five intensity ratios of Fig. 4 are either those defined by Axelrod or their inverse (for later convenience), and these are plotted against the optical ratio NA/*n* for the three objectives used. More recent FPM studies (e.g., Blackman et al., 1996) have employed other quantities based on these intensity ratios, i.e., Legendre polynomials, but the original notation of Axelrod is certainly intuitive and most accessible for direct comparison. Also shown in Fig. 4 are theoretical predictions for intensity ratios based on a combination of optical factors and molecular parameters. The crucial optical factors are NA/*n* and also the arc, or angle γ_0, subtended at the edge as it is projected into the small pixeled images of points *B* and *C*. Important molecular parameters include: the product of rotational diffusion and fluorescence lifetime, $D\tau$, as the molecule rotates through an azimuthal angle $\Delta\eta$ before emission; and the angles θ_a and θ_e for, respectively, orientations of the absorption and emission dipoles relative to the bilayer's local tangent plane. The curves of Fig. 4 are calculated using much of the same set of values that Axelrod used in fully mobile probe calculations where the fluorescence absorption and emission dipoles were modeled on a sphere; for the interested reader, the specific set of equations used from Axelrod (1979) were Eqs. 2, 3, 5, and 18–21. Parameters in common with the present results include $D\tau = 0.27$, $\theta_a = 28°$, and $\gamma_0 = 17.2°$; however, $\theta_e = 16°$ is specified here, and, though it differs from the 0° of Axelrod, it does satisfy our results for immobilized dye that indicate $|\theta_a - \theta_e| \lesssim 10°$.

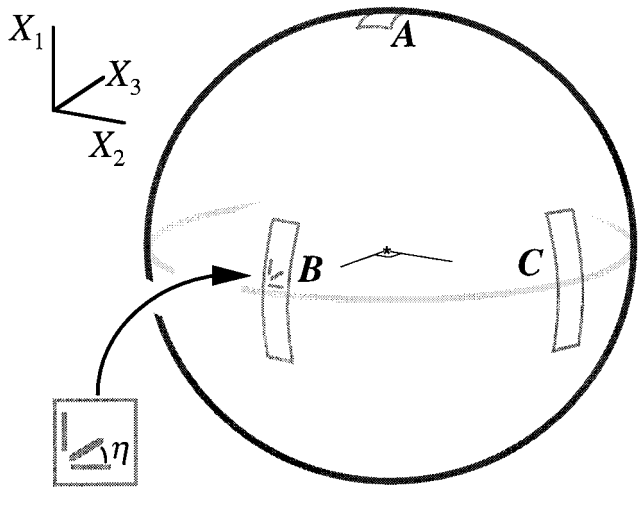

FIGURE 3 Optical frame perspective and regions of interest on a sphere. The optical axis of the microscope defines the X_1 direction, and the excitation beam is always polarized parallel to X_3. The origin of the triad is taken to be in the focal plane. A molecular dipole or filament in region *B* and parallel to the indicated equatorial plane is also parallel to the axis X_2; whereas a filament in region *C* that is parallel to the indicated equatorial plane is parallel to the axis X_3. The angle η denotes an azimuthal measure around the local normal to the bilayer's tangent plane; for $\theta = 0$, η is measured in the tangent plane. Although a symmetric distribution about the local normal may be expected, such symmetry is broken in a planar image of the sphere. Absolute orientations at the key points on the sphere must therefore be defined. At points *A* and *C*, the X_3-direction provides a convenient datum defining $\eta = 0$; at point *B*, the X_2-direction provides a convenient datum.

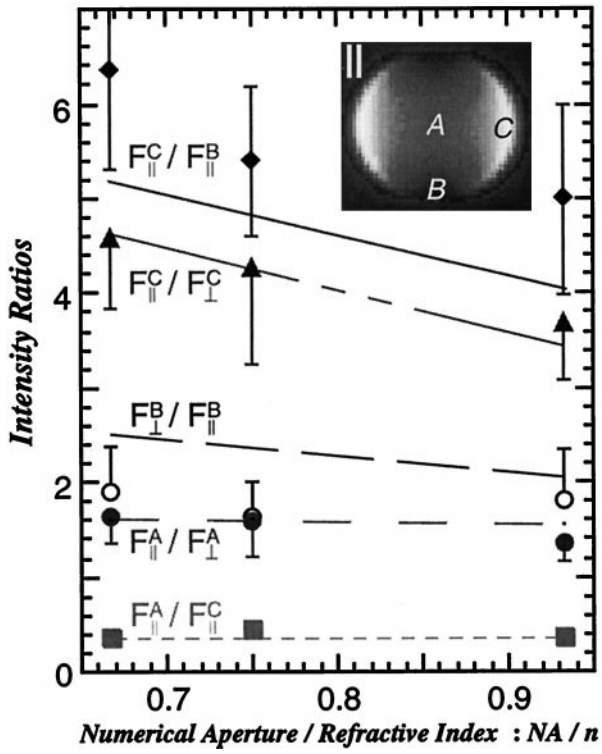

FIGURE 4 Characteristic fluorescence intensity ratios versus aperture factor, NA/*n*, for diI-labeled, sphered red cell ghosts. The inset image is taken with parallel polarizers for excitation and emission, and the labeling scheme follows that of Fig. 3. The experimental points and error bars at a given NA/*n* are for more than 10 cells examined with each of three objectives, from left to right: (NA = 1.0, 40 × oil), (NA = 0.75, 40 × dry), (NA = 1.4, 60 × oil). The theoretical curves follow the theory of Axelrod (1979) with molecular and optical parameters described in the Methods section. The sphere's diameter is 6.5 μm.

As pointed out by Axelrod, the largest experimental errors are generally associated with the point having the lowest edge intensities: point *B*. Nonetheless, the present results with diI demonstrate both the capability of the polarizer-based imaging system and an agreement between theory and experiment for this model system at a level of ≲20%.

RESULTS

FPM of rhodamine phalloidin-labeled protofilaments in a sphered ghost

Flaccid red cell ghosts (Fig. 5 *A*), labeled with rhodamine phalloidin and viewed at ~23°C through parallel polarizers,

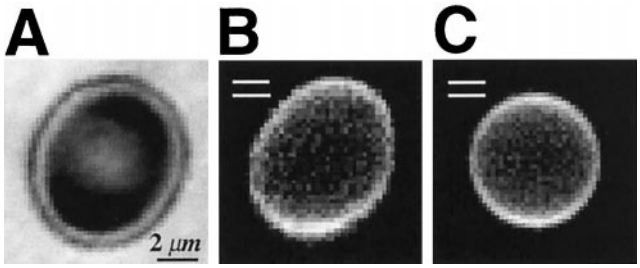

FIGURE 5 Rhodamine-phalloidin labeled, discocytic ghost at 23°C as observed in (*A*) brightfield or in (*B*) fluorescence with parallel polarizers. (*C*), Osmotically-sphered ghost at 37°C as observed in fluorescence with parallel polarizers.

appeared, at a strictly qualitative level, very much like diI. Maximum intensity occurs at those regions of the edge-bright images that are relatively parallel to the polarizers (Fig. 5 *B*). Sphering the ghosts and heating to 37°C had no qualitative effect on the polarization image (Fig. 5 *C*). These results suggest that sphering the membrane does not strongly reorient protofilaments and that heating does not strongly randomize their orientations. Sphering does minimize, however, cell-to-cell variations in intensity measurements, as recognized by Axelrod. Maximum intensities of the rhodamine phalloidin-labeled cells studied here were much lower than intensities with diI labeling, despite qualitatively similar distributions. This limits the range of objective lenses that could be used in FPM of rhodamine phalloidin. The minimum intensity and corresponding minimum rhodamine phalloidin concentration is, however, the regime most desirable to work in for determining actin orientation at the membrane because this regime maximizes the bound to free ratio of phalloidin inside the cell.

Quantitation of FPM images demonstrates that the relative polarization between the characteristic points *A*, *B*, and *C* on a sphere (Fig. 6) differ for labeled actin versus diI. Table 1 lists the various intensity ratios—the same ratios previously identified for diI. These are tabulated together with both the source of rhodamine phalloidin and the optics used (i.e., NA). Results are given for different isotypes of rhodamine phalloidin: MP, Sigma, or the thin layer chromatography (TLC)-separated peak 2 isomer(s). Each column entry represents a mean and standard deviation of measurements pooled together between vertical and horizontal polarizers in the same way as diI. Even allowing for differences between optics and probe source, it is very clear that the ratios with rhodamine phalloidin, which span the range from 0.37 to 2.5, are not as spread as the values seen with diI that range from 0.35 to 6.0 (Fig. 4). This may seem to suggest, simplistically, that actin protofilaments are not quite as tangent to the membrane as the headgroup of diI. However, the more accurate statement is that the reduced polarization with actin reflects a reduced degree of alignment of rhodamine phalloidin—a compound that labels helical actin and not a flat bilayer like diI. This distinction will be clarified purposefully in both further Results and Discussion.

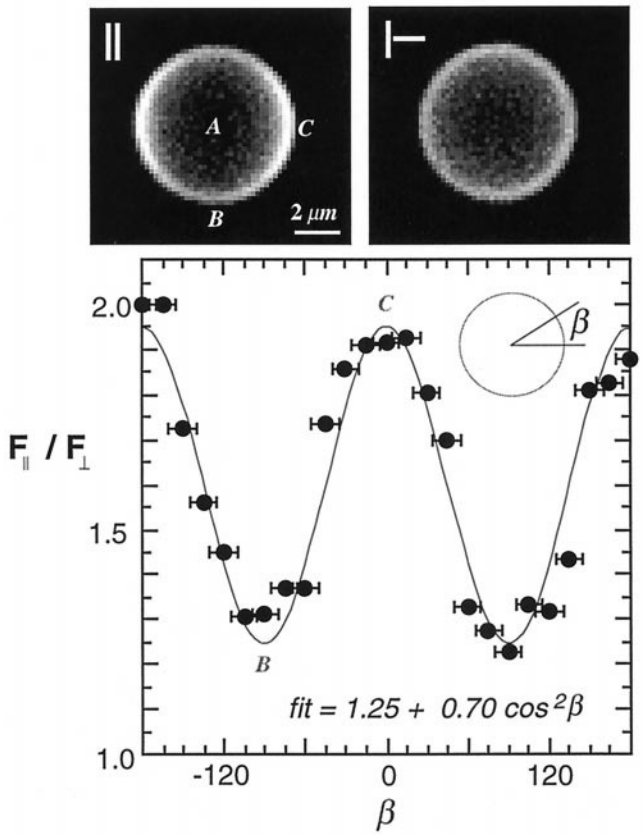

FIGURE 6 Polarization images of sphered red blood cells labeled with rhodamine phalloidin and obtained for a fixed excitation polarization (NA = 1.0, 40 × objective). The emission polarizer is either parallel and denoted by ∥, or crossed and denoted by ⊢. Points on the sphere are labeled according to the convention of Figs. 3 and 4 where the excitation direction is always tangent to point *C*. The plot shows the variation of the parallel: crossed polarizer intensity ratio along the edge contour of paired images of labeled spheres. Point C corresponds to $\beta = 0°$. Peak intensities were used here at angles accurate to $\pm 5°$.

In comparing the results within any given column of Table 1, differences are apparent between different optics and different probes. The most significant experimental determinant appears to be TLC purification. It is possible that enhanced polarization can be furthered by preparation with either the 5- or 6-isomer of TRITC, which are both undoubtedly in this peak. Such approaches have been taken in recent studies of myosin orientation on actin filaments (Sabido-David et al., 1998). However, any entry in Table 1 differs from its respective bottom-line collective average by no more 15–20%. Though the differences may be statistically significant, the lack of strong systematic variation suggests that real differences are truly small. For a perspective, a review of the diI data in Fig. 4, shows overlapping error bars for the same ratio determined from different optics; the predicted trends, nonetheless, generally track the averages well. For these reasons and reasons of completeness in this first study of actin protofilament orientation, the entire set of actin data has been tabulated, but later interpretation and discussion of these results will exclusively emphasize the bottom-line collective averages of Table 1.

TABLE 1 Mean intensity ratios for rhodamine phalloidin-labeled, sphered red blood cell ghosts using two objectives and the several isotypes of probe

	$F_{\parallel}^{A}/F_{\perp}^{A}$	$F_{\perp}^{B}/F_{\parallel}^{B}$	$F_{\parallel}^{C}/F_{\perp}^{C}$	$F_{\parallel}^{A}/F_{\parallel}^{C}$	$F_{\parallel}^{C}/F_{\parallel}^{B}$
NA 1.0					
MP (18 cells)	1.49 ± 0.09	0.77 ± 0.11	1.71 ± 0.18	0.44 ± 0.03	1.17 ± 0.06
Sigma (16 cells)	1.51 ± 0.15	0.80 ± 0.09	1.90 ± 0.27	0.44 ± 0.06	1.42 ± 0.13
peak 2 (16 cells)	1.91 ± 0.11	0.67 ± 0.05	2.54 ± 0.25	0.55 ± 0.05	1.54 ± 0.10
NA 1.4					
MP (15 cells)	1.45 ± 0.25	0.71 ± 0.11	1.79 ± 0.26	0.48 ± 0.07	1.21 ± 0.03
Sigma (19 cells)	1.69 ± 0.23	0.84 ± 0.12	2.17 ± 0.30	0.38 ± 0.06	1.55 ± 0.10
Average	1.62 ± 0.17	0.76 ± 0.10	2.02 ± 0.25	0.46 ± 0.04	1.38 ± 0.08

Finally, an examination of the peak intensity variation around the edge of the sphere's contour suggested combining the raw intensities into ratios (plot in Fig. 6). Peaks correspond to the ratio $F_{\parallel}^{C}/F_{\perp}^{C}$, and valleys correspond to the ratio $F_{\parallel}^{B}/F_{\perp}^{B}$. These extremes reinforce the idea that points *B* and *C* are the characteristic points along the membrane contour. They also provide a database for simplified examination of the angle dependence of polarization ratios, as will be elaborated upon in the Discussion section.

FPM of single actin filaments

Lorenz et al. (1993) have modeled at atomic resolution the interaction of phalloidin along the actin filament. It is clear from that effort, and it is also to be expected simply from the known helical structure of F-actin that rhodamine phalloidin orientation on a filament, with respect to a plane parallel to the filament axis, exists in a number of average orientation states that is essentially given by the number of subunits per period of the filament. This is intrinsically unlike diI, which integrates into the membrane so that each diI molecule appears essentially like any other over a short time given by $D\tau = 0.27$ (see Methods section). Of course, the relevant rotational diffusion time of diI enters into the modeling of polarization, but one does not expect a dominant multitude of immobile states as is understood to be the case for bound phalloidin. Because of this difference between labeled actin and diI, polarization intensities obtained from single actin filaments were essential experimental measurements to make with our FPM system.

Actin filaments polymerized in the presence of rhodamine-labeled phalloidin were examined by FPM in a closed chamber containing an oxygen depleting enzyme system (Kishino and Yanagida, 1988). Due to the absence of oxygen, photobleaching was minimal during the collection of a sequence of polarization images. Single filaments with axes roughly parallel or perpendicular to the excitation polarizer are shown in Fig. 7 *A*. A difference in the images is very clear and indicates that the absorption and emission dipoles of the fluorophore are relatively more parallel than perpendicular to the filament axis, as others have also found (Kinosita et al., 1991, 1988; Borejdo and Burlacu, 1994; Zhukarev et al., 1995). At a qualitative level, this immediately suggests for the actin-labeled red cells imaged with parallel polarizers (e.g., Fig. 5) that the actin protofilaments are approximately tangent to the surface rather than normal. If the protofilaments were predominantly normal to the lipid bilayer, then the intensity at point *B* on the sphere would be higher than the intensity at point *C*—the opposite is found.

The seed of the argument just planted will be further elaborated in a quantitative, empirically-based discussion based on relative intensities extracted from the various polarization images. The relevant ratios for actin filaments oriented in the X_2–X_3 plane are tabulated in Table 2. In the column headings, the first subscript refers to the axis of the filament in this plane relative to the X_3-axis of polarized excitation. The second subscript refers to the direction of the emission polarizer either parallel (∥) or perpendicular (⊥) to the excitation direction. Inasmuch as the excitation polarizer, either vertically or horizontally oriented in the lab frame, always defines the X_3-axis, it does not appear in the subscripts. Of note, the filament intensities for the four arrangements of polarizers were each divided by the sum total of the four intensities (per Zhukarev et al., 1995) to achieve a simple normalization for intracomparison. The results are easily summarized. For excitation and emission polarizers (both parallel to the filament axis), detected intensities averaged ~2.4 higher than excitation and emission polarizers (both perpendicular to the filament axis). Crossed polarizers gave results only slightly different from the re-

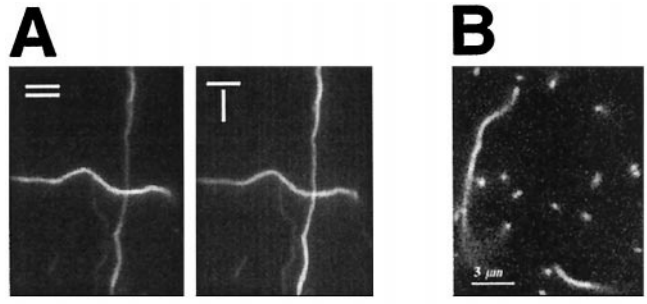

FIGURE 7 Single actin filaments observed on or near the coverslip with NA = 1.4, 60 × oil objective. (*A*) Polarization images with both parallel excitation/emission polarizers or parallel excitation/crossed emission polarizers. (*B*) Spots are filaments oriented roughly along the X_1-axis and viewed without polarizers ~1–2 μm above the coverslip. The scale bar applies to all images.

TABLE 2 Single actin filament intensities (normalized in sum) from four polarization images of each filament in the X_2–X_3 plane

	${}_{X3}I_{\parallel}$	${}_{X3}I_{\perp}$	${}_{X2}I_{\perp}$	${}_{X2}I_{\parallel}$
NA 1.4				
Sigma (8 filam.)	0.43 ± 0.02	0.17 ± 0.01	0.19 ± 0.02	0.21 ± 0.02
peak 2 (7 filam.)	0.46 ± 0.03	0.17 ± 0.01	0.19 ± 0.02	0.21 ± 0.02
NA 1.0				
Sigma (7 filam.)	0.45 ± 0.05	0.17 ± 0.03	0.18 ± 0.02	0.20 ± 0.02
peak 2 (7 filam.)	0.46 ± 0.03	0.17 ± 0.04	0.17 ± 0.03	0.20 ± 0.04
Average	0.45 ± 0.03	0.17 ± 0.02	0.18 ± 0.02	0.21 ± 0.02

sults with both polarizers parallel but oriented perpendicular to the filament. As with the sphered red cells, NA and probe source appear to have little effect in the measurements. Later discussion will therefore use the bottom-line averages of Table 2.

As suggested by the schematic of filaments on a sphere in Fig. 3, filaments oriented orthogonal to the X_2–X_3 plane are potential contributors to the total polarization signal. FPM measures of polarization were therefore attempted with $\sim X_1$-aligned filaments (Fig. 7 *B*). Such an orientation of many-micron-long filaments was achieved between two coverslips minimally separated ($\sim$50 μm) and with no polylysine coating; under these conditions, a significant fraction of filaments spontaneously tethered to the glass at one end. By focusing $\sim$1–2 μm above the coverslip, direct imaging of the ill-defined tethering orientation was avoided. In focusing further above the coverslip, filament motion and blurring attenuated the signal. The latter finding simply reflects the filament persistence length, which others have estimated to be in excess of several microns. After verifying extension of a filament into the bulk, FPM was therefore confined to just above the coverslip where thermal motion was minimal and spots corresponding to $\sim X_1$-aligned filaments could be easily identified within and between images. The primary intensity ratio that resulted from these efforts was

$$({}_{X1}I_{\parallel}/{}_{X1}I_{\perp}) = 1.35 \pm 0.14 \quad (6 \text{ filaments}).$$

A final measurement made on individual filaments involved an explicit evaluation of the effect of the angular variable η, azimuthal about the optical axis. This is identifiable with point *A* in Fig. 3, provided one ignores out-of-focus effects. For various filaments or extended portions of filaments in the X_2–X_3 plane and oriented at an angle η with respect to X_3, the parallel:crossed intensity ratio was determined (Fig. 8). The limit states of $\eta = 0°$ and $\eta = 90°$ correspond to more reliably determined ratios listed in Table 2, $({}_{X3}I_{\parallel}/{}_{X3}I_{\perp})$ and $({}_{X2}I_{\parallel}/{}_{X2}I_{\perp})$, respectively. The shifted cosine-squared curve-fit accurately captures these limits and also coarsely reflects the variation with angle. It is physically motivated by the cosine-squared dependence of bare emission intensities on angles formed between a single emission dipole and the optical frame axes (Eq. 1 in Axelrod, 1979). Such an empirical interpolation between limit states, together with Table 2 and the ratio $({}_{X1}I_{\parallel}/{}_{X1}I_{\perp})$, will soon form the foundation for elucidating filament orientation in sphered red cells.

Finally, images of a large number of filaments all stuck to the coverslip and randomly arranged in the X_2–X_3 plane were taken with both parallel and crossed polarizers. By integrating intensities after background subtraction, these ensembles of actin filaments yield a ratio $({}_{ensem}I_{\parallel}/{}_{ensem}I_{\perp}) = 1.39 \pm 0.13$. As will be elaborated later, this ratio is within 20% of the quantity $(F_{\parallel}^{A}/F_{\perp}^{A}) = 1.62 \pm 0.17$ in Table 1, suggesting that filaments are randomly oriented at point *A*, provided out-of-focus effects are again ignored in the spirit of Axelrod (1979).

DISCUSSION

The FPM results suggest, at a qualitative level, that actin protofilaments in sphered cells are relatively more tangent than normal in orientation to the membrane. This is because isolated filaments that are labeled with any of several rhodamine phalloidin probes fluoresce far brighter when both excited and viewed through polarizers parallel to the filament axis. Clearly, if all filaments were oriented normal to the membrane, the intensity at point *B* in the image would be greater than the intensity at point *C* rather than the inverse, as found. The results are not overly sensitive to the variant of rhodamine phalloidin used; nor are they strongly influenced by objective aperture, even though FPM generally is sensitive to such optical factors as shown experimentally with diI. After a brief discussion below of probe

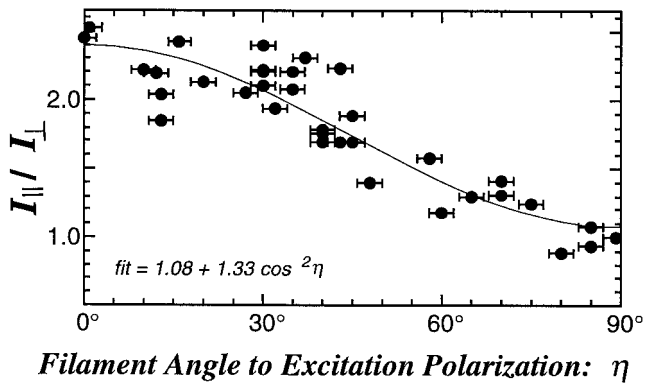

FIGURE 8 Polarization ratio for more than 30 individual actin filaments, or portions of actin filaments, oriented with respect to the excitation direction. All filaments were in the X_2–X_3 plane, but oriented at an angle η with respect to the X_3-direction. The error in this angle measurement is $\sim$5°; Table 2 suggests error bars in the intensity ratios of $\sim$5–15%.

orientation on filaments, a more quantitative but simple demonstration of the tangent orientation of actin to the red cell membrane is given. This is achieved by suitably fitting the single filament results to the membrane results, noting that both sets of data were obtained with the same FPM system and that aperture and probe effects are neglected.

Orientation of rhodamine phalloidin on isolated F-actin

Prior FPM analyses of rhodamine phalloidin-labeled actin filaments have yielded a range of values for probe orientation. Using a probe that presumably corresponds to isotype MP (Fig. 2 *A*), Kinosita et al. (1991) concluded that the nearly colinear absorption and emission dipoles (colinear within 10°—Tregear and Mendelson, 1975) of the probe are inclined at an angle of 25° to 37° with respect to a straight filament axis. These prior results appeared essentially independent of association with myosin; the helical nature of probe binding to F-actin would, however, tend to decrease the inclination angle. With a mixture of rhodamine phalloidin isotypes shown in Fig. 2 *B*, Borejdo and Burlacu (1994) concluded that the probes' dipoles are inclined at an angle reportedly within a few degrees of 50° for either a helical arrangement or a Gaussian distribution of probe on the filament. The measurement was made in the presence of either ATP or bound myosin; freely-suspended filaments appeared to yield a broader distribution of width ~20° in the Gaussian model. Comparison of our raw polarization measurements for single filaments to these prior reports yield intermediate orientations for the probe on F-actin.

Filament Ensemble Model with uniform $\theta_i = \theta$

Due to the complications of probe variation and the heterogeneous orientations of probe along the helical actin filament, a semi-empirical analysis will be given for the orientations of actin protofilaments at the membranes of red cell spheres. The average single filament results, in large part summarized at the bottom of Table 2, will be used in combination with geometric, optical, and statistical averaging as a basis for understanding the membrane results at the bottom of Table 1. Since the membrane values reflect a local ensemble of filaments, the analyses presented will all be referred to as the Filament Ensemble Model.

For the *i*th filament, the model assumes a random azimuthal angle η_i ($0 \le \eta_i \le \pi$); that is, $P(\eta_i) = \pi^{-1}$. This seems justified because thermal rotations of protofilaments will be only weakly constrained by the approximately six connecting spectrin chains. The weakness of the constraints is expected because a spectrin chain undergoes fluctuations in its end-to-end length, at least in isolation, of order $\sim\sqrt{(bl)} \approx 50$ nm—a number based on the persistence length $b \sim 20$ nm and a contour length $l \sim 200$ nm (e.g., Discher et al., 1998). It must be noted, however, that, in contrast to molecular diI, such random rotations of supramolecular protofilaments are expected to be slow on the time scale of fluorescence lifetimes, eliminating explicit dynamics from FPM. In the initial analyses, a single filament angle θ will also be assumed for all filaments of the membrane, i.e., $\theta_i = \theta$ for $i = 1$ to $\sim 3 \times 10^5$ filaments. The probability distribution, $P(\theta_i)$, may thus be written as

$$P(\theta_i) = \delta(\theta_i - \theta). \tag{1}$$

Additional distributions will be considered in a separate subsection, but discussions will be intimately based on results of this simplest distribution.

To outline the theory, we will first exhaustively consider a membrane tangent orientation, i.e., $\theta = 0°$; this assumption will then be lifted, and $\theta = 45°$ or 90° considered. In comparing model predictions to experimental measurements (bottom of Table 1), quantitative agreement within ~17% will be sought. Such a margin of error would be comparable to that found in Axelrod (1979) where the difference averaged 17% between the best-fit theory and averages of experimental ratios determined for (five) sphered ghosts (e.g., Fig. 4).

The analysis begins by simplifying the single filament results of Table 2 to just two non-normalized values:

$$_{x3}I_{\parallel} = 2.4$$

and (2)

$$_{x3}I_{\perp} \approx {}_{x2}I_{\perp} \approx {}_{x2}I_{\parallel} \approx 1.0.$$

The latter equalities are within the collective standard errors. In seeking to explain the five averages listed at the bottom of Table 1, explicit optical correction factors will be largely neglected except for the single ratio involving two points, *A* and *C*, not in the same spatial plane. This approach incorporates the fact that single filament results already include some optical effects, and both Tables 1 and 2 show further effects of NA to be minimal. As shown in the Methods section, this was not the case for diI. The essential physics retained in the model presented here is that an emission intensity that is maximum in one filament orientation will decrease as the filament is rotated according to the direction cosine squared from that position. This is reflected in the simple cosine-squared fits of intensity ratios for both spheres and single filaments in Figs. 6 and 8, respectively. Recalling that $\theta = 0°$ is being assumed for initial presentation, the population average in a region *A*, *B*, or *C* in Fig. 3 is then just a suitable average over the angles η_i. By such a scheme, the five independent ratios are calculated below and compared to experiment in the order of simplicity of argument.

For the ratio ($F_{\parallel}^{C}/F_{\parallel}^{B}$) in Table 1, the calculation requires consideration of one physically obvious limit state. When filaments in regions *B* and *C* are oriented parallel to the optical axis X_1 ($\eta = \pi/2$), the emission intensity must be the same: setting $_{X1}I_{\parallel}^{(C)}/_{X1}I_{\parallel}^{(B)} = 1.0$ thus simply represents translational invariance. Next, rotating a filament in each of these regions to the state $\eta = 0$, the relative intensity ratio

of these now orthogonal filaments increases to 2.4. It is next assumed that there are a total of N filaments in each of regions B and C, and these can be paired 1:1 between each region as filaments having the same η_i. The desired ratio is then simply the number average of filament intensity ratios spanning the above two limit states, $\eta_i = 0$ and $\eta_i = \pi/2$. Again, for an angle η_i between two such states, experimental results motivated an interpolating formula of the form $[c_1 + c_2 \cos^2\eta_i]$ for the intensity ratios. For the present ratio, this leads to

$$\frac{F_\parallel^C}{F_\parallel^B} = \frac{1}{N}\sum_{i=1}^{N}\left[\frac{{}_{X1}I_\parallel^{(C)}}{{}_{X1}I_\parallel^{(B)}} + \left(\frac{{}_{X3}I_\parallel}{{}_{X2}I_\perp} - \frac{{}_{X1}I_\parallel^{(C)}}{{}_{X1}I_\parallel^{(B)}}\right)\cos^2\eta_i\right]$$

$$= \left(\frac{\pi}{2}\right)^{-1}\int_0^{\pi/2}\left[\frac{{}_{X1}I_\parallel^{(C)}}{{}_{X1}I_\parallel^{(B)}} + \left(\frac{{}_{X3}I_\parallel}{{}_{X2}I_\perp} - \frac{{}_{X1}I_\parallel^{(C)}}{{}_{X1}I_\parallel^{(B)}}\right)\cos^2\eta\right]d\eta$$

$$\approx \left(\frac{\pi}{2}\right)^{-1}\int_0^{\pi/2}[1.0 + (2.4 - 1.0)\cos^2\eta]\,d\eta$$

$$= 1.7.$$

Throughout both regions B and C, filaments with $\eta = \pi/2$ are considered essentially parallel to X_1. The error in angle in this assumption is of order 20° for the relevant objectives (essentially $\gamma_0 = 17.2°$ in Axelrod). The summation in the first line relies on the random η_i assumption, and the sum was made continuous in the second line by considering that the areas B and C either contain a large number of filament orientation angles, η_i, or that thermal averaging accomplishes the same end. Since the red cell membrane has $\sim 3 \times 10^4$ protofilaments, or $\sim 250/\mu m^2$, the approximate number of filaments viewed in all the various regions of area no smaller than $\sim 0.1\ \mu m^2$ is sufficiently large, especially if ensemble averaging applies. The final numerical prediction for $(F_\parallel^C/F_\parallel^B) = 1.7$ differs by 24% from the mean of the experimentally measured ratio, which Table 1 gives as 1.38 ± 0.08. Note that the integration simply leads to a prediction that is the average of the two limit states. This simple average turns out to be the worst among the ratios, but the error would be reduced if account were taken of the membrane curvature, which tends to decrease $F_\parallel^C$, because $\eta_i = \pi/2$ filaments contribute crossed polarizer signal, and also increase $F_\parallel^B$, because $\eta_i = \pi/2$ filaments contribute parallel polarizer signal. As outlined in Appendix 1, these contributions are comparatively weak and decrease the error from 24 to 19%.

Similar integrals to those above will be constructed for the remaining four ratios of Table 1 by interpolating between identifiable limit states associated with different single-filament intensity ratios. First, considering the ratio $(F_\parallel^A/F_\perp^A)$, the picture is essentially one in which filaments are randomly oriented in a plane; out-of-plane defocusing effects should be self-canceling in this ratio. As shown in the Results section, this picture is a very good approximation because integrations of imaged ensembles of actin filaments stuck to a coverslip yield a ratio for ${}_{ensem}I_\parallel/{}_{ensem}I_\perp = 1.39 \pm 0.13$, which compares well with the $(F_\parallel^A/F_\perp^A) = 1.62 \pm 0.17$ in Table 1. This picture suggests limit states corresponding to $\eta_i = 0$ and $\pi/2$ and given, respectively, by ${}_{X3}I_\parallel/{}_{X3}I_\perp = 2.4$ and ${}_{X2}I_\parallel/{}_{X2}I_\perp = 1.0$. The relevant integral and its evaluation are:

$$\frac{F_\parallel^A}{F_\perp^A} = \left(\frac{\pi}{2}\right)^{-1}\int_0^{\pi/2}\left[\frac{{}_{X2}I_\parallel}{{}_{X2}I_\perp} + \left(\frac{{}_{X3}I_\parallel}{{}_{X3}I_\perp} - \frac{{}_{X2}I_\parallel}{{}_{X2}I_\perp}\right)\cos^2\eta\right]d\eta$$

$$= 1.7$$

This model result is clearly within the margins of experimental error.

The ratio $(F_\parallel^C/F_\perp^C)$ involves a limit state for $\eta_i = \pi/2$ that requires the ratio $({}_{X1}I_\parallel/{}_{X1}I_\perp)$. This measurement, albeit difficult to make, was shown with single filaments to be $\sim 1.35 \pm 0.14$. The limit state for $\eta_i = 0$ is simply $({}_{X3}I_\parallel/{}_{X3}I_\perp) = 2.4$. Therefore, the relevant integral is

$$\frac{F_\parallel^C}{F_\perp^C} = \left(\frac{\pi}{2}\right)^{-1}\int_0^{\pi/2}\left[\frac{{}_{X1}I_\parallel}{{}_{X1}I_\perp} + \left(\frac{{}_{X3}I_\parallel}{{}_{X3}I_\parallel} - \frac{{}_{X1}I_\parallel}{{}_{X1}I_\perp}\right)^{-1}\right]\cos^2\eta\,d\eta$$

$$= 1.95$$

This model result is essentially the same as that given in Table 2 for this ratio: 2.02 ± 0.25.

The ratio $(F_\perp^B/F_\parallel^B)$ involves a limit state for $\eta_i = \pi/2$ that requires the ratio $({}_{X1}I_\perp/{}_{X1}I_\parallel)$, simply the inverse of the stated experimental result for a vertical filament. The limit state for $\eta_i = 0$ is simply $({}_{X2}I_\perp/{}_{X2}I_\parallel) = 1.0$. The relevant integral is

$$\frac{F_\perp^B}{F_\parallel^B} = \left(\frac{2}{\pi}\right)^{-1}\int_0^{\pi/2}\left[\left(\frac{{}_{X1}I_\parallel}{{}_{X1}I_\perp}\right)^{-1} + \left(\frac{{}_{X2}I_\perp}{{}_{X2}I_\parallel} - \left(\frac{{}_{X1}I_\parallel}{{}_{X1}I_\perp}\right)^{-1}\right)\cos^2\eta\right]d\eta$$

$$= 0.87.$$

This model result is essentially within the margins of experimental error given in Table 1 as 0.76 ± 0.10.

The fifth and final ratio to consider is $(F_\parallel^A/F_\parallel^C)$, which Axelrod (1979) described as the ratio most affected by the out-of-focus effect that tends to decrease the intensity from point A. Based on diffraction theory, this was accounted for by multiplying the theoretical prediction by $\phi \sim 1.33$. In addition, and as suggested by Fig. 3, many more filaments are observed at the edge position C than at A, simply due to geometry. The one-to-one pairing must be multiplied by a suitable degeneracy factor. Symmetry must not be forgotten, however: an equal number of filaments antipodal to region A also contribute to images of A. This should be incorporated in the original summation as an area ratio factor, $(2\ Area_A/Area_C)$. With image plane pixelation of ~ 300 nm, the subtended arc (γ_o in Axelrod) leads to an area ratio $(2\ Area_A/Area_C) \sim 0.4$. That these corrections are

valid is borne out by the inverse product $[\phi(2\ \mathrm{Area_A}/\mathrm{Area_C})]^{-1} = 1.88$, which compares extremely well with the unpolarized membrane:edge ratio of 1.85 ± 0.1 for rhodamine phalloidin-labeled ghosts. Now to define the limit state ratios. For $\eta_i = 0$, $({}_{X3}I_{\parallel}^{(A)}/{}_{X3}I_{\parallel}^{(C)}) = 1.0$. The limit state for $\eta_i = \pi/2$ requires speculating on the unmeasured ratio $({}_{X2}I_{\parallel}/{}_{X1}I_{\parallel})$. This is accomplished by first considering the ratio $({}_{X3}I_{\parallel}/{}_{X1}I_{\parallel})$, another unmeasured quantity, but one that is reasonably well estimated. Since the rhodamine group's dipoles must certainly be oriented at an acute angle with respect to the filament axis, a circularly symmetric distribution of probes around the axis implies that nearly all probe molecules are excited for an ${}_{X3}I_{\parallel}$ orientation of filament but (very) roughly half are excluded for an ${}_{X1}I_{\parallel}$ orientation. It is therefore postulated that $({}_{X3}I_{\parallel}/{}_{X1}I_{\parallel}) \sim 2$. This allows an estimate of the originally desired ratio $({}_{X2}I_{\parallel}/{}_{X1}I_{\parallel}) = ({}_{X3}I_{\parallel}/{}_{X1}I_{\parallel}) * ({}_{X2}I_{\parallel}/{}_{X3}I_{\parallel}) = 2 * 1/2.4 = 0.83$.

Finally, with the second limit state identified, and the initially determined factor of $[\phi(2\ \mathrm{Area_A}/\mathrm{Area_C})]$, the relevant integral is

$$\frac{F_{\parallel}^{A}}{F_{\parallel}^{C}} = \phi\left(\frac{2\ \mathrm{Area_A}}{\mathrm{Area_C}}\right) * \left(\frac{\pi}{2}\right)^{-1} \int_0^{\pi/2} \left[\frac{{}_{X2}I_{\parallel}}{{}_{X1}I_{\parallel}} + \left(\frac{{}_{X3}I_{\parallel}^{(A)}}{{}_{X3}I_{\parallel}^{(C)}} - \frac{{}_{X2}I_{\parallel}}{{}_{X1}I_{\parallel}}\right)\cos^2\eta\right] d\eta = 0.49.$$

This model result is again within the margins of experimental error given in Table 1 as 0.46 ± 0.04. This last model result and all of the above $\theta = 0°$ estimations are collected in Table 3. It is readily estimated from these tabulations that the mean error between model and experiment ratios is 9–10%. Finally, the approximations for single-filament ratios in Eq. 2 may be replaced with the more precise proportionalities of Table 2; carrying out the analysis above once more, the mean error among all the FPM ratios increases only slightly to 11%.

A quality of fit is also obtainable by applying the filament ensemble model to the two nontangent angles, $\theta = 90°$ and $\theta = 45°$. For brevity, only the ratio $(F_{\parallel}^{C}/F_{\perp}^{C})$ is developed here in a linear analysis of filament orientations; all five ratios are, however, elaborated in Appendix 2. For the ratio $(F_{\parallel}^{C}/F_{\perp}^{C})$, the tangent model, i.e., $\theta = 0°$, gave 1.95, a value essentially identical to the experimental determination of 2.02 ± 0.25. In contrast, for protofilaments always oriented exactly normal to the membrane, $(F_{\parallel}^{C}/F_{\perp}^{C})\big|_{\theta=\pi/2} = {}_{X2}I_{\parallel}/{}_{X2}I_{\perp} = 1.0 \pm 0.1$. This is clearly a poor fit; similar poor fits of experiment are obtained with other polarization ratios (Table 3). The second orientation considered is one in which all protofilaments make an angle $\theta = 45°$ with respect to the membrane. At point *C*, we postulate that two limit states need to be interpolated: 1) the filament is in the X_2–X_3 plane, and 2) the filament is in an X_1–X_2 plane. For case 1, the arguments above indicate that this limit state has a value that is $\frac{1}{2}[{}_{X2}I_{\parallel}/{}_{X2}I_{\perp} + {}_{X3}I_{\parallel}/{}_{X3}I_{\perp}] = 1.7$. For case 2, previous arguments indicate that this limit state has a value that is $\frac{1}{2}[{}_{X1}I_{\parallel}/{}_{X1}I_{\perp} + {}_{X2}I_{\parallel}/{}_{X2}I_{\perp}] = 1.18$. A simple estimate is thus made from the average of these two limiting cases: $(F_{\parallel}^{C}/F_{\perp}^{C})\big|_{\theta=\pi/4} = \frac{1}{2}(1.7 + 1.18) = 1.44$, which is still considerably outside the experimental range and correlates with simply being midway between the $\theta = 0°$ and $\theta = 90°$ results.

All of the above results are cumulated in Fig. 9 as the percent error between each model and the experimental ratios for membranes. An average error and standard deviation for all five ratios is also calculated and graphically illustrated. When fit to a line, this yields

$$\langle \%\mathrm{Error} \rangle = 8.4\% + 0.39\% \times \theta\,°. \tag{3}$$

This correlation readily allows an estimate of the angle, which limits the error between model and experiment to better than the sought for average of ≈17%: that angle is $\theta \lesssim 22°$.

In sum, a model in which actin protofilaments are all oriented tangent to the red cell membrane yields integrable interpolations between measured or well-estimated limit states and thereby provides optimal agreement with experimental FPM ratios. In subsequent discussion, allowance is made for nonsingular distributions of protofilaments. The linear fit for ⟨%Error⟩ obtained with $P(\theta_i) = \delta(\theta_i - \theta)$, i.e., Eq. 3, is used to estimate the error introduced through broadly distributed $P(\theta_i)$.

Filament ensemble model with either $\theta_{min} \le \theta_i \le \theta_{max}$ or Gaussian θ_i

Recalling that θ_i must fall within the range $0° \le \theta_i \le 90°$, the first normalized $P(\theta_i)$ to be considered is a simple subset,

$$\begin{aligned} P(\theta_i) &= (\theta_{max} - \theta_{min})^{-1} \quad \text{if} \quad \theta_{min} \le \theta_i \le \theta_{max}, \\ P(\theta_i) &= 0 \qquad\qquad\quad \text{if} \quad \theta_{min} \ge \theta_i,\ \theta_i \ge \theta_{max}. \end{aligned} \tag{4}$$

TABLE 3 Mean intensity ratios calculated by the filament ensemble model for images of sphered red cells

θ	$F_{\parallel}^{A}/F_{\perp}^{A}$	$F_{\perp}^{B}/F_{\parallel}^{B}$	$F_{\parallel}^{C}/F_{\perp}^{C}$	$F_{\parallel}^{A}/F_{\parallel}^{C}$	$F_{\parallel}^{C}/F_{\parallel}^{B}$
90 °	1.35 ± 0.14	0.42	1.0 ± 0.1	0.64	0.42
45 °	1.53	0.56	1.44	0.56	0.85
0 °	1.7 (1.7)*	0.87 (0.81)	1.95 (1.85)	0.49 (0.49)	1.7 (1.65)
Experiment	1.62 ± 0.17	0.76 ± 0.10	2.02 ± 0.25	0.46 ± 0.04	1.38 ± 0.08

*Numbers in parentheses estimated with finite: $\gamma_0 = 30°$.

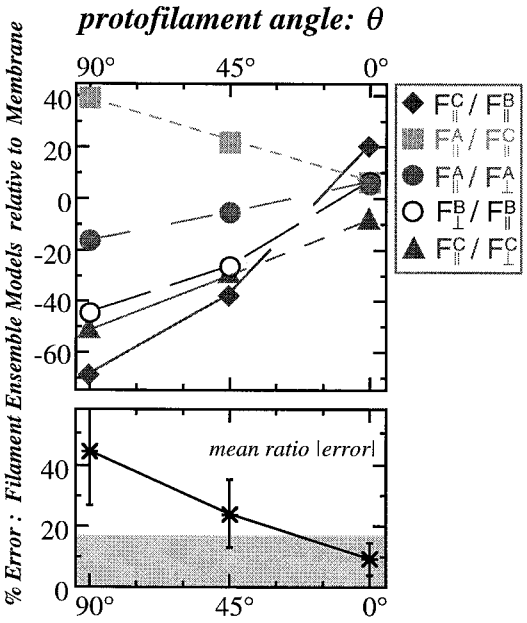

FIGURE 9 Relative differences between filament ensemble model estimates for polarization ratios and experimental, membrane measures as tabulated in Table 3 for three protofilament angles. The lower plot illustrates the average absolute error with ±S.D. of the ratios. The shaded zone indicates the typical range of error that might be expected in these types of fluorescence polarization measurements.

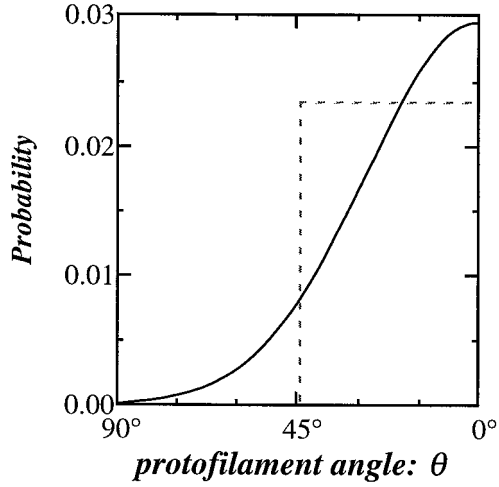

FIGURE 10 Square and Gaussian distributions that yield a mean error of 17% between these filament ensemble models and experiment. The error is smaller for narrower, more peaked distributions.

This square distribution includes a completely random θ_i, where $\theta_{min} = 0°$ and $\theta_{max} = 90°$. It is straightforward to then use Eq. 3 and estimate the mean error between model and experiment for such a distribution of completely random protofilaments. For random θ_i, this is just

$$\langle \%\text{Error} \rangle = 8.4\% + 0.39\% \times 45° = 26\%.$$

This is well outside the tolerable range of average error. Indeed, to achieve a $\langle \%\text{Error} \rangle \approx 17\%$ with $\theta_{min} = 0°$, it is required that $\theta_{max} = 44°$. This simple, bounding distribution is illustrated in Fig. 10. Half of the protofilaments in this distribution satisfy, of course, $0° \leq \theta_i \leq 22°$.

The square distribution above seems far less physical than one that is Gaussian in θ_i. Assuming first a probability distribution peaked at $\theta = 0°$,

$$P(\theta_i) = C^{-1}\exp(-\tfrac{1}{2}\,\theta_i^2/\langle \delta\theta_i^2 \rangle), \qquad (5)$$

where $\langle \delta\theta_i^2 \rangle$ is the variance and the normalizing constant $C = [(\pi/4)\langle \delta\theta_i^2 \rangle]^{1/2}\ \mathrm{erf}[(\pi/2)/\langle \delta\theta_i^2 \rangle^{1/2}]$. Consistent units of radians or degrees are, of course, used. The error function is numerically limited to values no smaller than $\mathrm{erf}(1) \approx 0.84$. Calculating the mean error for this distribution can therefore be shown to yield

$$\langle \%\text{Error} \rangle = \int_0^{\pi/2} P(\theta_i)[8.4\% + 0.39\% \times \theta\,°]\,d\theta$$

$$\approx 8.4\% + 0.39\% \times (\langle \delta\theta_i^2 \rangle/\pi)^{1/2}.$$

To once more obtain a mean error no greater than $\langle \%\text{Error} \rangle \approx 17\%$ between all measurements and the model requires that the root mean variance of the distribution be bounded: $\langle \delta\theta_i^2 \rangle^{1/2} \lesssim 39°$. However, more than 60% of the Gaussian distribution is within the interval $0° \leq \theta_i \leq 22°$. The Gaussian variance is somewhat smaller than the square distribution width of $\theta_{max} = 44°$ because the Gaussian $P(\theta_i)$ includes large angle states missing from the square distribution, as is evident in Fig. 10. It must be emphasized that narrower distributions would fit the experiments proportionately better. It should also be pointed out that Gaussian distributions centered off of $\theta = \theta_c = 0°$ might also be considered. However, to limit the error to less than 17%, such distributions must become infinitely narrow as θ_c increases to 22°; this is implied by the analysis at the end of the last section.

The results thus implicate a significant constraining role on actin protofilament orientation. The constraints may be exerted at the membrane, very possibly it seems, via a multiunit complex involving protein 4.1 and the transmembrane protein glycophorin C (Fig. 11).

Constraint compliance of vertical linkages

Recall that a protofilament's azimuthal angle, η_i, was argued to be random $P(\eta_i) = \pi^{-1}$ $(0 \leq \eta_i \leq \pi)$ because such rotations will not be significantly constrained by the thermally-soft spectrin chains constituting horizontal linkages. A similar, fluctuation analysis proves insightful for the second, out-of-plane Euler angle, θ_i, and demonstrates that the Gaussian $P(\theta_i)$ above is more than just statistics. This distribution is trivially derived from a rotational energy, quadratic in form, $\mathscr{E}_i = \tfrac{1}{2}k_\theta \delta\theta_i^2$, where k_θ is a torsional spring constant associated with the compliance of vertical linkages such as those arising with Glycophorin C. Indeed,

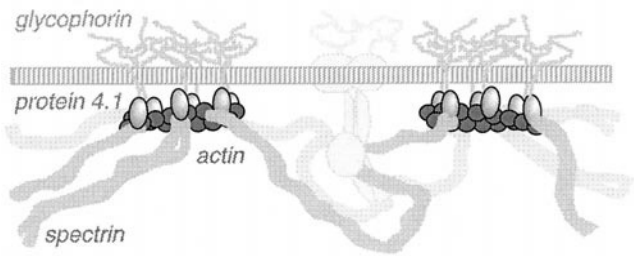

FIGURE 11 Speculative schematic of the red cell membrane's spectrin-actin network including protein 4.1 and the transmembrane protein Glycophorin C. Assemblies with these two proteins are proposed to strongly influence the tangent orientation of the actin protofilament. Omitted are many additional integral and peripheral membrane proteins. Given the approximate size and shape of protein 4.1 and the distance estimate of 5–8 nm between the middle of 4.1 and the inner surface of the bilayer (Shahrokh et al., 1991), actin filaments should lie roughly parallel and within 10–20 nm of the inner surface of the bilayer.

$P(\theta_i)$ is immediately obtained as a Boltzmann weight in $\mathscr{E}_i$, i.e., $\exp(-\mathscr{E}_i/k_BT)$, with appeal to the equipartition theorem,

$$\tfrac{1}{2}\, k_\theta \langle \delta\theta_i^2 \rangle = \tfrac{1}{2}\, k_B T.$$

Moreover, since the root mean variance of θ_i was shown to be bounded by the measurement error to $\leq 39°$, the compliance of the constraining interaction can also be estimated. Converting the variance to radians, it is estimated that $k_\theta = k_BT/\langle \delta\theta_i^2 \rangle \leq 2.2\ k_BT$, where $k_BT = 4 \times 10^{-21}$ J.

Inasmuch as the actin protofilament may be considered rigid over its extremely short length, the torsional spring constant reflects the distributed compliance of the proteins linking the filament to the bilayer (Fig. 11). A suitable moment arm is the protofilament length (~35 nm) which yields a thermally-driven see-saw action of the protofilament of root mean amplitude ≤22 nm. Such a fluctuation amplitude appears high in light of an energy transfer distance for protein 4.1 bound to the membrane via Glycophorin C—a distance reported to be 8 nm (Shahrokh et al., 1991). Because this length scale is well within the bounding error, it seems more reasonable to assume it to be the amplitude of thermal fluctuation. Thus, converting 8 nm to a root mean variance and then a torsional spring constant yields, respectively, $\langle \delta\theta_i^2 \rangle^{1/2} \approx 13°$ and $k_\theta \approx 19 k_BT$. Further, dividing this k_θ by the square of the moment arm, again approximated by the protofilament length, the effective spring composed of $n = 2$ to 5 complexes in parallel is estimated to be $k_{(4.1\cdot glyC)n} \geq 0.06$ mN/m. Finally, dividing by the number of complexes, an effective spring constant ≳0.01 mN/m is obtained for a single 4.1·glycophorin complex. For comparison, the effective spring constant for spectrin is in the range of $k_{spectrin} \sim 0.001–0.01$ mN/m (Discher et al., 1998). In contrast, the effective spring constant of a single 5-nm-long helix, e.g., the transmembrane domain of Glycophorin C, has been estimated with ideal polypeptides to be in the range $k_{helix} \sim 2000–4000$ mN/m (Suezaki and Go, 1976). The best estimate therefore indicates that the linkage between actin and membrane is stiffer than the laterally connected mesh of spectrin, but not nearly so stiff as, say, a membrane-spanning helix.

Finally, a true measure of $\langle \delta\theta_i^2 \rangle$ would, of course, provide better insight into the nature of protofilament constraint. The coarse numbers at hand merely outline the significance. In addition, it would be of comparable value to determine the azimuthal fluctuations, $\delta\eta_i$ (Fig. 1 *B*). These should, in principle, be larger in magnitude, reflecting the relative softness of thermally fluctuating spectrin chains.

CONCLUSIONS

Physically-motivated application of single filament FPM results to the interpretation of images of sphered, actin-labeled red cells yields a self-consistent molecular scale picture in which protofilaments are oriented essentially tangent to the membrane. Error analyses, including consideration of Gaussian and square distributions, qualifies the majority of angles to ≲22° from the tangent plane. In coming to this conclusion, it is assumed that the protofilaments are otherwise randomly distributed in the tangent plane—a notion consistent with a soft, thermally-fluctuating network implicit in the k_BT-driven polymer motions first posited by Evans (1975). Extending this view, rotational fluctuations of rigid protofilaments are coupled to elastic fluctuations of spectrin and, it seems likely, hydrodynamic dissipation in the lipid bilayer. Furthermore, protofilaments held tangent by Glycophorin C and protein 4.1 should form an impenetrable barrier to membrane protein diffusion. Accounting for this steric obstacle of significant dimension may be necessary to understand past and present studies using particle tracking or fluorescence recovery after photobleaching.

The finding that red cell actin is oriented tangent to the membrane points to a number of avenues for further investigation. First, since actin is a structural component at the membrane, FPM coupled to controlled deformation of the membrane—micropipette aspiration, for example—would seem particularly relevant to assessing the extent of microrotation (Discher et al., 1998) that locally accompanies anisotropic stretching of the network (Discher and Mohandas, 1996). The same set of questions also applies to both the outer hair cell, with its extended filaments of actin, and actin-vesicle systems, which show spontaneously ordered actin filaments at the membrane. Of note, the outer hair cell has recently been examined by fluorescence imaged micropipette deformation (Oghalai et al., 1998), extending to this system the method originally developed for the red cell (Discher et al., 1994). Physically related to such deformation studies, the time-scale and extent of thermal rotations of protofilaments might be deduced from time-resolved phosphorence decay (e.g., Tsuji et al., 1988) applied to fluorescent probes such as eosin phalloidin. At a simpler structural level, the examination of rhodamine phalloidin-labeled membranes deficient in glycophorin C, protein 4.1, or Band 3 could help clarify the role of these molecules in actin filament attachment and orientation at the membrane. Spe-

cific inhibitors such as recombinant peptides of 4.1's spectrin–actin binding domain (Discher et al., 1995) or a C-terminal peptide of glycophorin C that binds protein 4.1 (Pinder et al., 1995) could also help clarity whether actin protofilaments are molecularly constrained by specific interactions at the red cell membrane.

APPENDIX 1

The effect of curvature in regions *B* and *C* may be estimated by linear analysis as illustrated here for the ratio $F_{\parallel}^{C}/F_{\parallel}^{B}$. The curvature of these regions is characterized by the included angle γ_0, which we consider, in the extreme, to be 30°; it is more realistically ~20°. First, noting that the filament ensemble model described in the text without curvature effects reduces, for the desired ratio, to the simple average,

$$\frac{F_{\parallel}^{C}}{F_{\parallel}^{B}} = \frac{1}{2}\left[\frac{x_1 I_{\parallel}^{(C)}}{x_1 I_{\parallel}^{(B)}} + \frac{x_3 I_{\parallel}}{x_2 I_{\perp}}\right].$$

Only the first term is affected by curvature, and this is simply approximated by breaking it up into an angle weighted sum,

$$\begin{aligned}\frac{F_{\parallel}^{C}}{F_{\parallel}^{B}} &= \frac{1}{2}\left[\frac{\pi - \gamma_0}{\pi}\left(\frac{x_1 I_{\parallel}^{(C)}}{x_1 I_{\parallel}^{(B)}}\right) + \frac{\gamma_0}{\pi}\left(\frac{x_2 I_{\parallel}^{(C)}}{x_3 I_{\parallel}^{(B)}}\right) + \frac{x_3 I_{\parallel}}{x_2 I_{\perp}}\right] \\ &\approx \frac{1}{2}\left[\frac{5}{6}(1.0) + \frac{1}{6}(2.4)^{-1} + (2.4)\right] \\ &= 1.65.\end{aligned}$$

The primary geometric feature incorporated is that X_1-aligned filaments in the uncorrected model have, in fact, other components within a curved region of membrane. Diffraction is still ignored.

APPENDIX 2

For $\theta = 90°$,

$$\frac{F_{\parallel}^{A}}{F_{\perp}^{A}} = \left[\frac{x_1 I_{\parallel}}{x_1 I_{\perp}}\right]$$

$$\frac{F_{\parallel}^{B}}{F_{\perp}^{B}} = \left[\frac{x_3 I_{\parallel}}{x_3 I_{\perp}}\right]$$

$$\frac{F_{\parallel}^{A}}{F_{\parallel}^{C}} = \phi\left(\frac{2\,\mathrm{Area_A}}{\mathrm{Area_C}}\right)\left[\frac{x_1 I_{\parallel}}{x_2 I_{\parallel}}\right]$$

$$\frac{F_{\parallel}^{C}}{F_{\parallel}^{B}} = \left[\frac{x_2 I_{\parallel}}{x_3 I_{\parallel}}\right].$$

For $\theta = 45°$,

$$\frac{F_{\parallel}^{A}}{F_{\perp}^{A}} = \frac{1}{2}\left[\frac{1}{2}\left(\frac{x_3 I_{\parallel}}{x_3 I_{\perp}} + \frac{x_1 I_{\parallel}}{x_1 I_{\perp}}\right) + \frac{1}{2}\left(\frac{x_1 I_{\parallel}}{x_1 I_{\perp}} + \frac{x_2 I_{\parallel}}{x_2 I_{\perp}}\right)\right]$$

$$\frac{F_{\parallel}^{B}}{F_{\perp}^{B}} = \frac{1}{2}\left[\frac{1}{2}\left(\frac{x_1 I_{\parallel}}{x_1 I_{\perp}} + \frac{x_3 I_{\parallel}}{x_3 I_{\perp}}\right) + \frac{1}{2}\left(\frac{x_2 I_{\parallel}}{x_2 I_{\perp}} + \frac{x_3 I_{\parallel}}{x_3 I_{\perp}}\right)\right]$$

$$\frac{F_{\parallel}^{A}}{F_{\parallel}^{C}} = \phi\left(\frac{2\,\mathrm{Area_A}}{\mathrm{Area_C}}\right) \times \frac{1}{2}\left[\frac{1}{2}\left(\frac{x_1 I_{\parallel}}{x_1 I_{\parallel}} + \frac{x_2 I_{\parallel}}{x_2 I_{\parallel}}\right) + \frac{1}{2}\left(\frac{x_1 I_{\parallel}}{x_2 I_{\parallel}} + \frac{x_3 I_{\parallel}}{x_3 I_{\parallel}}\right)\right]$$

$$\frac{F_{\parallel}^{C}}{F_{\parallel}^{B}} = \frac{1}{2}\left[\frac{1}{2}\left(\frac{x_2 I_{\parallel}}{x_2 I_{\parallel}} + \frac{x_3 I_{\parallel}}{x_3 I_{\parallel}}\right) + \frac{1}{2}\left(\frac{x_1 I_{\parallel}}{x_1 I_{\parallel}} + \frac{x_2 I_{\parallel}}{x_3 I_{\parallel}}\right)\right].$$

The authors wish to thank Prof. Henry Shuman, Prof. Yale Goldman, Dr. Vladimir Zhukarev, and the Sanger Laboratory for the valued help and early discussions concerning fluorescence polarization. The authors also acknowledge the careful reading of the manuscript by Dr. Uulke van der Heide and Prof. Shuman. This work was supported in part by the Whitaker Foundation (DD), National Institutes of Health R01-HL62352–01 (DD), and by the Fondation pour la Recherche Medicale (CP).

REFERENCES

Alloisio, N., N. Dalla Venezia, A. Rana, K. Andrabi, P. Texier, F. Gilsanz, J. P. Cartron, J. Delaunay, and A. H. Chishti. 1993. Evidence that red blood cell protein p55 may participate in the skeleton-membrane linkage that involves protein 4.1 and glycophorin C. *Blood*. 82:1323–1327.

Axelrod, D. 1979. Carbocyanine dye orientation in red cell membrane studied by microscopic fluorescence polarization. *Biophys. J.* 26: 557–574.

Bennett, V., and P. J. Stenbuck. 1979. The membrane attachment protein for spectrin is associated with band 3 in human erythrocyte membranes. *Nature*. 280:468–473.

Blackman, S. M., C. E. Cobb, A. H. Beth, and D. W. Piston. 1996. The orientation of eosin-5-maleimide on human erythrocyte band 3 measured by fluorescence polarization microscopy. *Biophys. J* 71:194–208.

Borejdo, J., and S. Burlacu. 1994. Orientation of actin filaments during motion in in vitro motility assay. *Biophys. J.* 66:1319–1327.

Byers, T. J., and D. Branton. 1985. Visualization of the protein associations in the erythrocyte membrane skeleton. *Proc. Natl. Acad. Sci. USA.* 82:6153–6157.

Discher, D. E., N. Mohandas, and E. A. Evans. 1994. Molecular maps of red cell deformation: hidden elasticity and in situ connectivity. *Science*. 266:1032–1035.

Discher, D. E., R. Winardi, P. O. Schischmanoff, M. Parra, J. G. Conboy, and N. Mohandas. 1995. Mechanochemistry of protein 4.1's spectin–actin binding domain: ternary complex interactions, membrane binding, network integration, structural strengthening. *J. Cell Biol.* 130: 897–907.

Discher, D. E., and N. Mohandas. 1996. Kinematics of red cell aspiration by fluorescence-imaged microdeformation. *Biophys. J* 71:1680–1694.

Discher, D. E., D. H. Boal, and S. K. Boey. 1998. Simulations of the erythrocyte cytoskeleton at large deformation. II. Micropipette aspiration. *Biophys. J.* 75:1584–1597.

Evans, E. A. 1975. Composite material structure of red cell membranes. *In* Erythrocyte Structure and Function. G. J. Brewer, editor. Liss, New York. 491–506.

Faulstich, H., S. Zobeley, G. Rinnerthaler, and J. V. Small. 1988. Fluorescent phallotoxins as probes for filamentous actin. *J. Muscle Res. Cell Mot.* 9:370–383.

Fowler, V. M. 1996. Regulation of actin filament length in erythrocytes and striated muscle. *Curr. Opin. Cell Biol.* 8:86–96.

Gicquaud, C. 1995. Does actin bind to membrane lipids under conditions compatible with those existing in vivo? *Biochem. Biophys. Res. Com.* 208:1154–1158.

Grimm, R., M. Barmann, W. Hackl, D. Typke, E. Sackmann, and W. Baumeister. 1997. Energy filtered electron tomography of ice-embedded actin and vesicles. *Biophys. J.* 72:482–489.

Holley, M. C., and J. F. Ashmore. 1990. Spectrin, actin and the structure of the cortical lattice in mammalian cochlear outer hair cells. *J. Cell Sci*. 96:283–291.

Kas, J., H. Strey, J. X. Tang, D. Finger, R. Ezzell, E. Sackmann, and P. A. Janmey. 1996. F-actin, a model polymer for semiflexible chains in dilute, semidilute, and liquid crystalline solutions. *Biophys. J.* 70: 609–625.

Kinosita, K., H. Itoh, Jr., S. Ishiwata, K. Hirano, T. Nishizaka, and T. Hayakawa. 1991. Dual-view microscopy with a single camera: real-time imaging of molecular orientations and calcium. *J. Cell Biol.* 115:67–73.

Kishino, A., and T. Yanagida. 1988. Force measurements by micromanipulation of a single actin filament by glass needles. *Nature.* 334:74–76.

Lieber, M. R., and T. L. Steck. 1989. Hemolytic holes in human erythrocyte membrane ghosts. *Meth. Enzymol.* 173:356–367.

Lorenz, M., D. Popp, and K. C. Holmes. 1993. Refinement of the F-actin model against x-ray fiber diffraction data by the use of a directed mutation algorithm. *J. Mol. Biol.* 234:826–836.

Mische, S. M., M. S. Mooseker, and J. S. Morrow. 1987. Erythrocyte adducin: a calmodulin-regulated actin-bundling protein that stimulates spectrin-actin binding. *J. Cell Biol.* 105:2837–2845.

Mohandas, N., and E. Evans. 1994. Mechanical properties of the red cell membrane in relation to molecular structure and genetic defects. *Ann. Rev. Biophys. Biomol. Struct.* 23:787–818.

Nash, G. B., J. Parmar, M. E. Reid. 1990. Effects of deficiencies of glycophorins C and D on the physical properties of the red cell. *Brit. J. Haemat.* 76:282–287.

Oghalai, J. S., A. A. Patel, T. Nakagawa, and W. E. Brownell. 1998. Fluorescence-imaged microdeformation of the outer hair cell lateral wall. *J. Neurosci.* 18:48–58.

Peters, L. L., R. A. Shivdasani, S. C. Liu, M. Hanspal, K. M. John, J. M. Gonzalez, C. Brugnara, B. Gwynn, N. Mohandas, S. L. Alper, S. H. Orkin, and S. E. Lux. 1996. Anion exchanger 1 (band 3) is required to prevent erythrocyte membrane surface loss but not to form the membrane skeleton. *Cell.* 86:917–927.

Pinder, J. C., B. Gardner, and W. B. Gratzer. 1995. Interaction of protein 4.1 with the red cell membrane: effects of phosphorylation by protein kinase C. *Biochem. Biophys. Res. Comm* 210:478–482.

Pradhan, D., P. Williamson, and R. A. Schlegel. Bilayer/cytoskeleton interactions in lipid-symmetric erythrocytes assessed by a photoactivable phospholipid analogue. 1991. *Biochemistry.* 30:7754–7758.

Reid, M. E., Y. Takakuwa, J. Conboy, G. Tchernia, and N. Mohandas. 1990. Glycophorin C content of human erythrocyte membrane is regulated by protein 4.1. *Blood*. 75:2229–2234.

Sabido-David, C., S. C. Hopkins, L. D. Saraswat, S. Lowey, Y. E. Goldman, and M. Irving. 1998. Orientation changes of fluorescent probes at five sites on the myosin regulatory light chain during contraction of single skeletal muscle fibres. *J. Mol. Biol.* 279:387–402.

Shahrokh, Z., A. S. Verkman, and S. B. Shohet. 1991. Distance between skeletal protein 4.1 and the erythrocyte membrane bilayer measured by resonance energy transfer. *J. Biol. Chem* 266:12082–12089.

Shen, B. W., R. Josephs, and T. L. Steck. 1986. Ultrastructure of the intact skeleton of the human erythrocyte membrane. *J. Cell. Biol.* 102: 997–1006.

Smythe, J., B. Gardner, and D. J. Anstee. 1994. Quantitation of the number of molecules of glycophorins C and D on normal red blood cells using radioiodinated Fab fragments of monoclonal antibodies. *Blood*. 83: 1668–1672.

Stockem, W., W. Naib-Majani, K. E. Wohlfarth-Bottermann, M. Osborn, and K. Weber. 1983. Pinocytosis and locomotion of amoebae. XIX. Immunocytochemical demonstration of actin and myosin in *Amoeba proteus*. *Eur. J. Cell. Bio.* 29:171–178.

Stokke, B. T., A. Mikkelsen, and A. Elgsaeter. 1986. Spectrin, human erythrocyte shapes, and mechanochemical properties. *Biophys. J.* 49: 319–327.

Southgate, C. D., A. H. Chishti, B. Mitchell, S. J. Yi, J. Palek. 1996. Targeted disruption of the murine erythroid band 3 gene results in spherocytosis and severe haemolytic anaemia despite a normal membrane skeleton. *Nat. Genet.* 14:227–230.

Suezaki, Y., and N. Go. 1976. Fluctuations and mechanical strength of alpha-helices of polyglycine and poly(L-alanine). *Biopolymers.* 15: 2137–2153.

Takakuwa, Y., G. Tchernia, M. Rossi, M. Benabadji, and N. Mohandas. 1986. Restoration of normal membrane stability to unstable protein 4.1-deficient erythrocyte membranes by incorporation of purified protein 4.1. *J. Clin. Invest.* 78:80–85.

Ting-Beall, H. P., A. S. Lee, and R. M. Hochmuth. 1995. Effect of cytochalasin D on the mechanical properties and morphology of passive human neutrophils. *Ann. Biomed. Eng*. 23:666–671.

Tregear, T. T., and M. Mendelson. 1975. Polarization from a helix of fluorophores and its relation to that obtained from muscle. *Biophys. J.* 15:455–466.

Tsuji, A., K. Kawasaki, S. Ohnishi, H. Merkle, and A. Kusumi. 1988. Regulation of band 3 mobilities in erythrocyte ghost membranes by protein association and cytoskeletal meshwork. *Biochemistry.* 27: 7447–7452.

Tyler, J. M., W. R. Hargreaves, and D. Branton. 1979. Purification of two spectrin-binding proteins: biochemical and electron microscopic evidence for site-specific reassociation between spectrin and bands 2.1 and 4.1. *Proc. Natl. Acad. Sci. USA*. 76:5192–5196.

Ursitti, J. A., and V. M. Fowler. 1994. Immunolocalization of tropomodulin, tropomyosin and actin in spread human erythrocyte skeletons. *J. Cell. Sci.* 107:1633–1639.

Waugh, R. E., and P. Agre. 1988. Reductions of erythrocyte membrane viscoelastic coefficients reflect spectrin deficiencies in hereditary spherocytosis. *J. Clin. Invest.* 81:133–141.

Zhukarev, V., F. Ashton, J. M. Sanger, J. W. Sanger, and H. Shuman. 1995. Organization and structure of actin filament bundles in listeria-infected cells. *Cell Motil. Cytoskelet*. 30:229–246.